IEEE Access
Multidisciplinary | Rapid Review | Open Access Journal

Received February 22, 2019, accepted March 4, 2019, date of publication March 11, 2019, date of current version March 26, 2019.

Digital Object Identifier 10.1109/ACCESS.2019.2904109

Battery-Less NFC Sensor for pH Monitoring

MARTI BOADA, ANTONIO LAZARO, (Senior Member, IEEE), RAMON VILLARINO, AND DAVID GIRBAU, (Senior Member, IEEE)
Department of Electronic, Electrical and Automatic Engineering, Universitat Rovira i Virgili, 43007 Tarragona, Spain

Corresponding author: Antonio Lazaro (antonioramon.lazaro@urv.cat)

This work was supported in part by the H2020 Grant Agreement 645771–EMERGENT, and in part by the Spanish Government Project TEC2015-67883-R and Grant BES-2016-077291.

ABSTRACT In this paper, we present a low-cost battery-less color sensor based on Near Field Communication (NFC). This system consists of a color sensor connected to a low-power microcontroller connected to an NFC chip. The energy needed to power up the chipset is retrieved from the magnetic field generated by the reader, i.e., a commercial smartphone. The low cost of NFC chips affords the opportunity to manufacture low-cost tags with sensing capability. We have developed a mobile application to simultaneously present the data and send them to a database in the cloud. The system has been tested with several pH reactive strips. The pH was determined via color measurement using the HSV color space. A simple linear relationship was found between the Hue parameter and the pH. Comparison with the pH determination via smartphone camera showed that the accuracy was greater when the NFC colorimeter was used.

INDEX TERMS Battery-less, color sensor, Near Field Communication, RFID, PH, energy harvesting.

I. INTRODUCTION

Microfluidic paper-based devices [1] for analyses based on color determination are widespread in applications such as medical devices [2], [3] and pH measurements [4]–[6]. The main advantages of these devices are that they are inexpensive, do not require an energy source, allow for easy transportation of fluids, and are easy to use. However, since diagnosis depends on optical measurements, accuracy is poor especially when, as in pH measurements, classification between different levels is required. PH measurement has a wide range of applications. It is used, for example, to check the water condition of swimming pools, tap water and aquariums. It is also used in medical applications such as sweat or saliva analysis and skin control in wounds, where it can indicate an infection before the infection becomes visible. However, as pH electronic probes are expensive and require continuous calibration, the cost is prohibitive for home applications. In medical applications (e.g. urine tests [7]), the probes need to be sterilized each time they are used in order to avoid contamination between samples. For this reason, paper-based color strips have been extended as the simplest and cheapest way to quickly indicate pH measurements. With the expansion of smartphones with high-quality integrated cameras, several methods for colorimeter measurement using smartphones have been proposed [3]–[6]. The main advantages of pH measurement using smartphone cameras are that these devices are inexpensive and portable. However, they have also important drawbacks. For example, the readout depends on ambient illumination and camera type and requires special image processing techniques, so there are variations between smartphone models and the programs used to process the images. To solve the problems related to ambient light condition variation, some studies propose the use of an enclosure to keep the sample in darkness just being illuminated by the smartphone cameras led [2], [5], [6]. This method permits the reading to be independent of the external light conditions. However, the absolute control of light conditioning is not possible since each camera uses a different led, so the color temperature and intensity may change, as well as the led location on the camera's enclosure, which makes the sample enclosure device-dependent.

pH is defined as the decimal logarithm of the reciprocal of the hydrogen ion activity in a solution [8]. Paper-based color strips change their color depending on the substances used to create the reactive. Some of the most common compounds used to create pH indicators are: phenolphthalein ($C_{20}H_{14}O_4$), which turns colorless in acidic solutions but pink in basic solutions; methyl red ($C_{15}H_{15}N_3O_2$), which is

The associate editor coordinating the review of this manuscript and approving it for publication was Mohamed Kheir.

red at a pH below 4.4 and yellow at a pH over 6.2; and thymol blue ($C_{27}H_{30}O_5S$), which turns red below pH 1.2, yellow between pH 2.8 and 8, and blue above 9.6. These substances are combined to react to a specific range of pH. Universal paper strips are mixtures of several pH indicators that extend the pH range over which they operate. The molecular geometry of these chemical compounds changes depending on the pH. This is due to modifications in the number of protons, which alter wavelength absorption and translate into a change of color.

Color evaluation has a wide field of applications. It can be used in medicaments doses control [9], glucose detection [10], water quality control [3], gas detection [11] or pH determination [5]. The most common way to digitalize the color for its further evaluation consists in using a photographic camera [2], [5], [6]. An alternative method for electronic color measurements is based on colorimeters. Colorimeters are tristimulus devices that use red, green, and blue filters to emulate the response of the human eye to light and color. Recently, low-cost colorimeters integrated into circuit devices have become commercially available and performed well. Low-cost colorimeters can therefore be designed for several applications [9]–[11]. Unlike the problems associated with smartphone cameras, color measurement by colorimeter has the advantage of repeatability due to a controlled light condition.

Near Field Communication (NFC) is a short-range Radiofrequency Identification system (RFID) that enables communication between devices using the ISM 13.56 MHz RFID band [12]. Although NFC has existed for over a decade [13], [14], this technology did not become popular until it was massively incorporated into payment systems. NFC technology enables simple and safe communication between electronic devices, thereby enabling consumers to perform contactless transactions, access digital content, and connect electronic devices with a single tap. For this reason, most smartphones now incorporate an NFC reader. NFC systems within the Internet of Things (IoT) and Industry 4.0 are therefore growing in importance [15]–[17]. NFC is also interesting for the development of low-cost sensors, since it provides a quick and easy way to obtain data from them simply by approaching the reader to the tag and without having to pair the devices.

Compared to other mobile-equipped wireless standards such as Bluetooth or Wi-Fi, NFC technology presents several advantages in short-range communications. NFC ICs are cheaper, and have capability to store data within the NFC IC, avoiding the use of microcontrollers or external memories, thus reducing price, complexity, size and power consumption. They also grant the possibility of developing low-cost sensors for a wide variety of applications. This is especially interesting for low-power sensors, powered by a small battery to store the sensed data on the NFC chip to be retrieved and analyzed afterwards by a computer [18].

One problem in IoT is the maintenance cost of the installations associated with replacing batteries in remote motes. Batteries need to be managed as a hazardous waste due to their toxic contents and reactive properties [19]. In this context, green electronics technology provides solutions that are well addressed to the broad needs of an energy-efficient society [20], [21].

The most important NFC IC manufacturers (TI, ST Microelectronics, NXP, AMS, and Melexis) have recently brought onto the market advanced integrated circuits (IC) with energy harvesting capabilities. These chips take some of the energy received by the magnetic field generated at the reader to provide an analog voltage output that can be used to power external electronics such as low-power microcontrollers and sensors. Some low-cost battery-less NFC sensors are found in the literature. The progressive introduction of these ICs into the market allows them to be commercially deployed for the development of low-cost battery-less portable sensors. In [22] a wide analysis of NFC energy harvesting capability is presented. Within the possibilities of using this feature, medical applications such as sensors for patient's body temperature [23], [24], sweat electrolyte [25] or pH wound monitoring [26], [27], gas detection tags [28] [11], soil-moisture sensors [17] and tire pressure systems [29] stand out.

Some references regarding pH monitoring systems based on NFC technology can be found in the literature. A low-power tag based on a SL13A chip from AMS, with potentiometric input to be used with pH and ion-selective electrodes is presented in [30]. A computer-based reader controls the sampling acquisition. A recent study [26] shows a medical application for wound care by measuring the color of a pH reactive compound located on a bandage. The color is measured using a photodiode and stored on a MLX90129 NFC chip with datalogger function from Melexis. These methods use a battery on the tag to sense the data and save it into the memory.

In this work we present a low-cost NFC-based system that combines an NFC IC for communications and a colorimeter IC with a microcontroller. The tag is completely passive and takes energy from the RF interrogating signal from the reader using the energy-harvesting capabilities of the NFC IC. A simple calibration method is used to convert the measured color of the pH strips into pH levels. We have developed a custom readout application that uses a smartphone with NFC compatibilities as a reader.

This paper is structured as follows. In section II we describe the system, in section III we analyze the signal processing for converting the measured color into pH, in section IV we present the experimental results we obtained with this system, and in section V we present our conclusions.

II. SYSTEM DESCRIPTION

A. SYSTEM OVERVIEW

An overview of the system is shown in Fig. 1. This consists of an electronic circuit made up of a color light-to-digital TCS3472 converter from TAOS [31], a white 4150 °K LED to illuminate the sample, a low-power Atmel Tiny

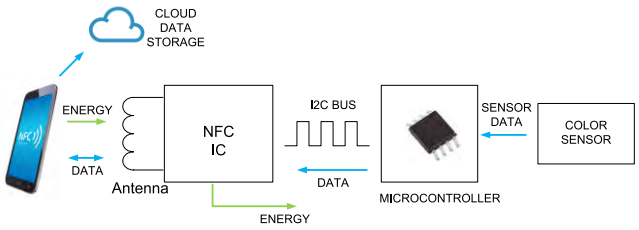

FIGURE 1. Block diagram of the proposed NFC-based pH sensor.

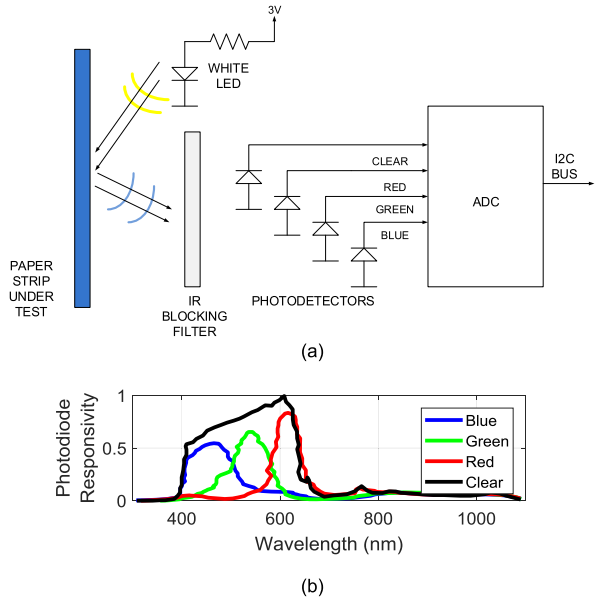

FIGURE 2. (a) Working principle of the colorimeter. (b) Spectral responsivity of the four channels.

85 microcontroller, and an NFC chip from ST Microelectronics (M24LR04E).

The TCS34725 has RGB and clear light sensing elements (Fig. 2). The TCS3472 light-to-digital converter contains a 3×4 photodiode array. The 3×4 photodiode array comprises red-filtered, green-filtered, blue-filtered, and clear (unfiltered) photodiodes. These photodiodes are coated with an IR-blocking filter that minimizes the IR spectral component of the incoming light and enables color measurements to be taken accurately. Spectral response curves of the four channels of the sensor is shown in Fig. 2b [31]. The four integrating ADCs simultaneously convert the amplified photodiode currents to a 16-bit digital value. These three chips are connected to each other via an I^2C bus. The NFC IC is connected to a PCB loop antenna, which works at 13.56 MHz, which corresponds to the NFC frequency standard.

The current consumption of each component is shown in Table 1. The NFC IC has four sink current configurable ranges. In this work, the mode with higher sink current (up to 5 mA) was selected to support the current need for the tag operation. A low-power Atmel 8-bit AVR ATtiny85 microcontroller was selected to be integrated into the prototype. This can be configured at different clock speeds and work

TABLE 1. Current consumption.

Component	Current consumption (μA)
M24LR04E	400
TCS34725	235
LED	2000
ATTiny85	300
TOTAL	**2935**

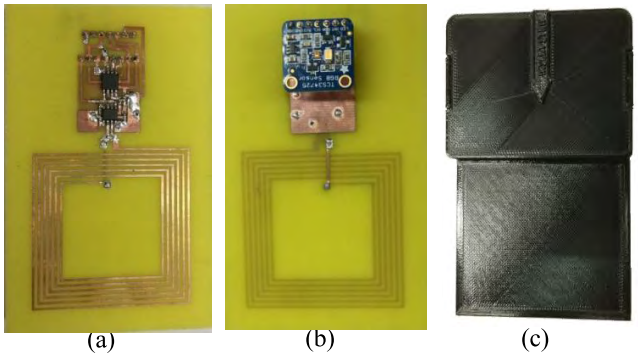

FIGURE 3. Photograph of the prototype from (a) the top and (b) the bottom and (c) the 3D printed enclosure.

down to 1.8V. Because of the power limitations presented by this system, it was configured to work at 1 MHz, where its consumption is around 300 μA at 3.3V. The total current consumption of the tag is about 3 mA which is less than the 5 mA that the NFC IC can harvest from the RF. Some of this consumption is due to the white LED used to illuminate the sample.

A photograph of the prototype is shown in Fig. 3. The loop antenna, the NFC IC and the microcontroller are located on the top, while the color sensor and the LED are connected on the bottom. The connector that links the two circuit boards is also used to download the firmware in the microcontroller. A plastic enclosure for the PCB was designed using a 3D printer (see Fig. 3b).

B. ANTENNA DESIGN AND ENERGY HARVESTING FROM THE SMARTPHONE READER

Wireless power transfer (WPT) between two coils has been widely studied [13], [14], [32], and [33]. NFC systems use the energy obtained from the coupling between two coils to feed the internal circuitry while performing the reading and writing operation through RF communications. In addition, NFC IC with energy harvesting capability includes a rectified voltage output to power up external circuits. Fig. 4 shows a model of the wireless power transfer between the reader and the tag. The reader antenna is characterized by the inductance (L_1) and its losses are modeled as a series-connected resistor (R_1). Besides, the reader includes a matching network. Therefore, it can be modeled using a Thevenin equivalent circuit with a voltage source and an output impedance, R_s. A series capacitance C_1 is added to make the circuit resonant at the operating

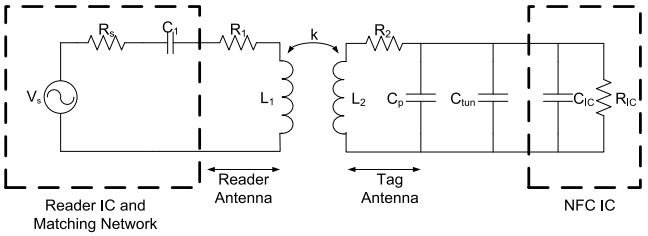

FIGURE 4. Wireless power transfer model between the reader and the tag.

frequency. The parasitics elements of the reader antenna have been taken into account in the matching network. The tag is composed by the antenna that is modeled as an inductance (L_2) in series with a loss resistance (R_2). A parasitic capacitance C_p is included to model the parasitics elements of the antenna. The NFC IC impedance is nonlinear and depends on the received power; it is modeled as a capacitance (C_{IC}) in parallel with a resistance (R_{IC}). A tuning capacitance C_{tun} is added to make the circuit resonant at the desired frequency. The 2-coil inductive link has been extensively analyzed in the literature (i.e. [32], [33]). Most of the studies are focused on the optimization of the system as a function of the quality factor of the coils, the coupling and the load resistance. However, the wireless power transfer in NFC systems imposes some restrictions. A matching network is required in the reader to reach the maximum transmission power, because the internal impedance of the reader IC is different to the antenna's impedance. An EMI filter is also inserted in order to reduce the interference due to harmonic emissions. The maximum value of the Q factor of the reader's antenna must be the -3 dB bandwidth B, which is equal to f_c/Q (being f_c the carrier frequency, 13.56 MHz), which is at least capable of channeling all the frequencies contained in the spectrum of the signal modulating the carrier frequency. The smartphone readers are designed to read a variety of standards such as ISO 14443A or ISO 15693. The maximum quality factor of the reader (Q_{1L}) is limited to 35 for the ISO1443A (the most restrictive case), and 100 for ISO15693 [14]. The loop antenna used in the reader presents a higher quality factor, and it is possible to reduce it adding series resistances. Analogously to the transmitter case, the quality factor of the tag (Q_{2L}) is limited to avoid the degradation of the modulation of the subcarrier. Therefore, the maximum value of Q_{2L} is approximately $Q_{2L} = 8\pi \approx 25$ [34]. The tag quality factor (Q_{2L}) is given by the hyperbolic average of the quality factor of the tag's antenna (Q_2) and the loaded quality factor of the IC's (Q_L):

$$Q_{2L} = \frac{1}{\frac{1}{Q_2} + \frac{1}{Q_L}} \approx Q_L \tag{1}$$

$$Q_L = \frac{R_{IC}}{\omega L_2} \tag{2}$$

The prototype is designed with a 50 mm × 50 mm square loop antenna printed on a FR4 PCB with a thickness of 0.8 mm and metallization thickness of 34 μm. In total there are six loops, with a width of 0.7 mm each one, and separated 1 mm one respect to the other. It was designed with a Keysight Momentum electromagnetic simulator. A tuning capacitance of 15 pF is added to the internal capacitance of the IC (27.5 pF) in order to adjust the resonance at 13.56 MHz in accordance with the expression:

$$f_r \approx \frac{1}{2\pi\sqrt{L_a\left(C_{IC} + C_p + C_{tun}\right)}} \tag{3}$$

where L_a is the tag's antenna inductance, C_{IC} is the internal IC capacitance (27.5 pF for M24LR04E), C_p is the layout parasitic capacitance (which includes the antenna capacitance and the parasitic capacitance due to the interconnections), and C_{tun} is the capacitor used to adjust the resonance frequency to the operation frequency f_c (13.56 MHz). Finally, the resonance frequency is verified with the Vector Network Analyzer measuring the S11 parameter with another loop antenna close to the tag.

The average magnetic field (H_{av}) received at the NFC tag must be above a threshold value (H_{min}) for a correct RF to DC conversion. H_{min} as a function of tag resonance frequency is obtained in (4) [34]:

$$H_{min} \approx \frac{\sqrt{\left[1 - \left(\frac{f}{f_r}\right)^2\right]^2 + \frac{1}{Q_{2L}^2}}}{2\pi f \mu_0 A \cdot N} \cdot U_{min} \tag{4}$$

where f_r is the resonance frequency of the tag, A is the loop area, N the number of loops and U_{min} is the minimum voltage required for the tag operation, which depends on the chip IC design and the used technology.

The average magnetic field (H_{av}) depends on the transmitted power at the reader and the coupling between the loop antennas. Therefore, it depends on the smartphone and its distance to the tag. In order to determine the threshold value H_{min} and the read range, some measurements have been performed. One of the tests consists of increasing the distance between the smartphone and the tag, while the resulting harvested DC voltage is monitored with an oscilloscope, and the correct reading of the color value with the smartphone application is checked. In order to determine the received H_{av} as a function of distance, the tag is replaced by a test loop antenna identical to the one used in the tag. The test antenna is connected to a spectrum analyzer to measure the received power at the carrier frequency. The impedance of the test antenna is measured using a vector network analyzer (VNA) for each distance. To avoid the coupling between the measurements of the impedance, the smartphone antenna is covered with a metal sheet. The average magnetic field can be calculated from the antenna factor (AF), obtained from the loop impedance [35]:

$$H_{av}(A_{RMS}/m) = V_{RMS} \cdot |AF| \tag{5}$$

$$AF = \frac{Z_0 + Z_{in}}{j2\pi f \mu_0 Z_0 A \cdot N} \tag{6}$$

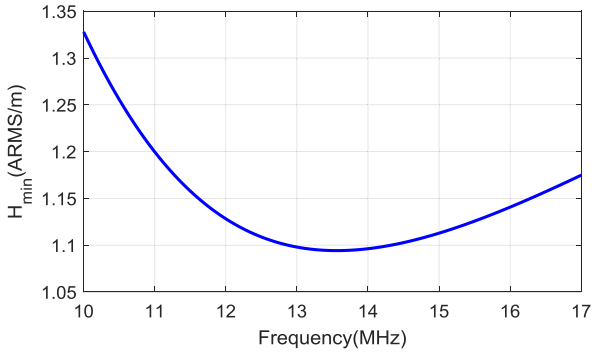

FIGURE 5. Calculated minimum magnetic field $H_{min}(A_{RMS}/m)$ as function of the frequency.

where Z_0 is the reference impedance (50 Ω) and Z_{in} is the input impedance of the antenna measured with the VNA. The root mean square voltage (V_{RMS}) is obtained from the power measured with a spectrum analyzer.

Fig. 5 shows the calculated H_{min}. It is considered a $R_{IC} = 450\ \Omega$ and $U_{min} = 4.8$V that is close to the voltage measured with an oscilloscope at the read range distance. Good agreement has been obtained with the experimental characterization of the H_{min} considering both models of smartphones.

In order to validate the performance of the system as a function of distance, several simulations using the model of Fig. 4 are done. Hence it is needed to know the main features of the antennas such as their coupling coefficient, k. The coupling coefficient of a pair of coils is a measure of the magnetic effect passing between them and therefore it is a fundamental parameter in NFC. It depends on the shape of the antennas, distance and alignment between antennas, and the materials. The coupling coefficient can be calculated from the Z parameters from electromagnetic simulations or S parameters measurements performed with VNA:

$$k = \frac{|Im(Z_{12})|}{\sqrt{Im\,(Z_{11}) \cdot Im(Z_{22})}} \tag{7}$$

It is known that the maximum coupling coefficient between two circular coils is obtained when the radius of the coils are the same [22]. This rule can be extrapolated for other shapes. The smartphone NFC antenna is mainly designed to read standard smart cards (53.98 mm × 85.60 mm). Therefore, a square coil of 50 mm was selected as the designed antenna for the prototypes since there are no special restrictions on the size. However, the coupling coefficient depends on the antenna implemented in the mobile.

Several simulations were performed to study the influence of the type of mobile antenna. In Fig. 6 some representative cases are shown.

Table 2 compares the main parameters depending on the chosen antenna. In the first case considered, the reader's and tag's antennae are identical (Antenna 1, Fig. 6a), it corresponds to the case of using a pc-based NFC reader (e.g. demonstration boards usually connected through USB) and is used as reference. As shown in Fig. 7, in this case the coupling coefficient is the highest. The second case (Antenna 2, Fig. 6b) corresponds to the same antenna as Fig. 6a but with a sheet of ferrite and a metal on the bottom plane. This is a selected case because it approximates a typical solution used in mobiles with a plastic case, where the NFC antenna is located over the battery with thin ferrite foils to isolate the antenna from the metallic parts [37]–[42], helping to reduce emissions interference from the internal mobile circuits. It can be observed in Table 2 that the effect of the ferrite increases the antenna's inductance by a factor μ_{ref} that depends on the magnetic permeability of the ferrite (μ_r) and the separation between the metal and the antenna's substrate. The definition of μ_{ref} is analogous to the relative effective permittivity taking into account the increase of the capacitance on an inhomogeneous transmission line [22]. Nowadays, commercial sintered ferrite sheets optimized to work at 13.56 MHz band can be found, such as Laird, TDK, or Würth Electronics, among others. These sheets achieve

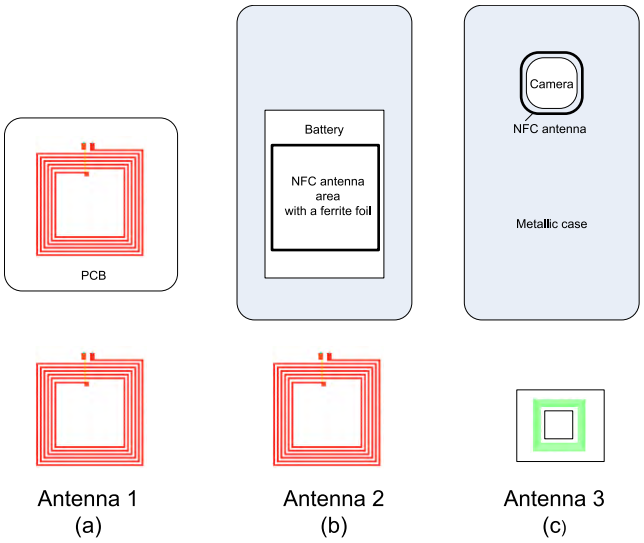

FIGURE 6. Different reader antennas. (a) Antenna over a PCB, (b) antenna over a mobile battery, and (c) antenna around the camera hole.

TABLE 2. Parameters of the Reader antennas.

Parameter	Antenna 1	Antenna 2	Antenna 3
Loop area (mm × mm)	50 × 50	50 × 50	25 × 25
Trace width (mm)	0.7	0.7	0.25
Spacing between traces (mm)	1	0.7	0.25
Substrate relative permittivity	4.7	4.7	3
Substrate thickness (mm)	0.8	0.8	0.1
Number of turns	6	6	8
Ferrite relative permeability	-	150-j5	150-j5
Inductance (μH)	2.68	3.92	3.63
Quality factor at 13.56 MHz	153	132	74
Self-resonance frequency (MHz)	77.0	37.4	79.05

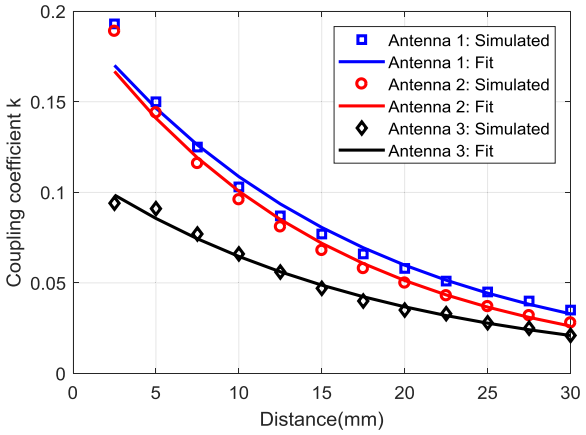

FIGURE 7. Simulated coupled coefficient for the reader antennas of Fig. 6. The fit obtained using a linear polynomial in log scale is compared (solid line).

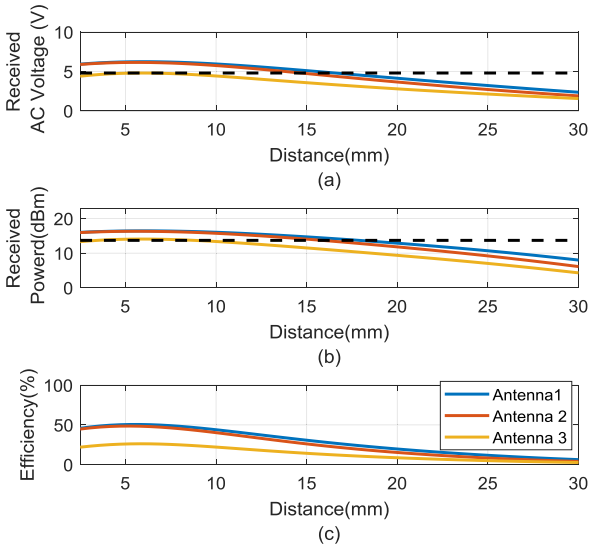

FIGURE 8. (a) Simulated voltage at the input of the tag at 13.56 MHz VAC, (b) simulated power at the tag and (c) efficiency, as a function of the distance for 20 dBm of transmission power. The threshold limit is shown in dashed line.

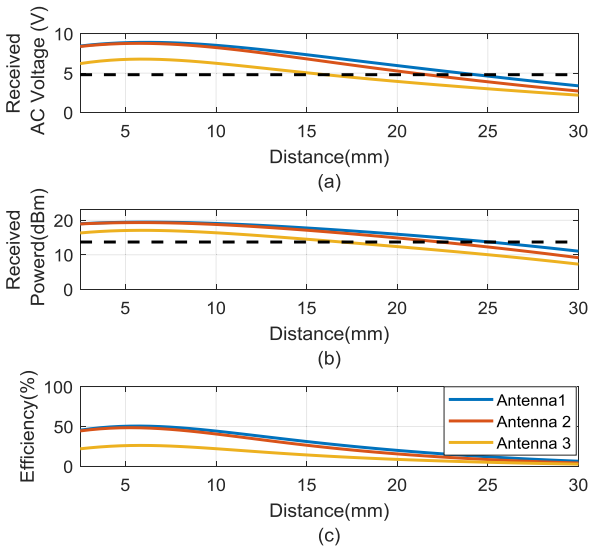

FIGURE 9. (a) Simulated voltage at the input of the tag at 13.56 MHz (V_{AC}), (b) simulated power at the tag and (c) efficiency, as a function of the distance for 23 dBm of transmission power. The threshold limit is shown in dashed line.

higher Re(μ_r), in the order of 100-190, and smaller Im(μ_r) loss, typically of 5-10 at 13.56 MHz, (e.g. MHLL12060-200 from Laird) than polymer absorber sheets. The tolerance of μ_r of ferrite foils can be $\pm$15-20%, which is translated to the tolerance in the antenna's inductance. The effect of the ferrite loss produces a reduction of the antenna quality factor as seen in Table 2.

The last case considered (Antenna 3, Fig. 6c) is known as Murata solution [43] and consists of the integration of the loop antenna around the hole of the camera. Several variation of this solution are frequently used with in smartphones with metallic cases [44]–[46]. A ferrite foil is also used to isolate the antenna from the metal case. Another similar solution used in some mobiles is proposed in [47] and [48] where the antenna is integrated at the top of the smartphone, on a plastic cover. In the simulations of the cases that use ferrite, a 100 μm thickness with 50 μm of adhesive plastic sheet of MHLL12060-200 from Laird (with $\mu_r = 150$-j5) is considered.

Fig. 7 compares the simulated coupling coefficient for each reader antenna as a function of the distance between the tag and reader antenna. The simulations have been done using Keysight Momentum. The coupling coefficient is obtained using (7) from the simulated Z parameters. A fit in logarithmic scale has been performed in order to enter the coupling as a function of the distance in the Keysight ADS circuit simulator. Fig. 7 shows a similar coupling coefficient for antennas 1 and 2 (Fig. 6a and 6b). Therefore, the introduction of the ferrite foil effectively mitigates the effect of the metal. On the other hand the coupling coefficient of Antenna 3 (Fig. 6c) is smaller than in the previous cases because its area is smaller too.

Some AC system simulations have been performed from the model of Fig. 4 using the Keysight ADS simulator. The voltages and currents (inserting current probes) at the relevant nodes of the circuit (antenna terminals) are computed by the simulator at 13.56 MHz. Figs. 8-9 show the voltage detected at the input of the tag (V_{AC}), the received power at the tag and the efficiency as a function of the distance between the reader and the tag.

Modern transceivers used in NFC mobiles can achieve transmission powers up to 23 dBm (eg. NXP PN7120 or TI TRF7960A). Therefore, a couple of values of transmission power are considered, 20 dBm and 23 dBm, addressed in Fig. 8 and Fig. 9, respectively, to compare its effect and foresee the possible losses in the matching network. A matching network with a final quality factor of the reader $Q_{1L} = 35$ is considered.

The nominal value (in the air) of the inductance and quality factor for the loop antenna designed in the prototype used are $L_2 = 2.8$ μH and $Q_2 = 153$, respectively. The tuning

TABLE 3. Read range of the Reader antennas.

Read Range (mm)	Antenna 1	Antenna 2	Antenna 3
Minimum (P_{TX}=20 dBm)	0	0	4
Maximum (P_{TX} =20 dBm)	17.3	15.1	8
Minimum (P_{TX} =23 dBm)	0	0	0
Maximum (P_{TX} =23 dBm)	24	21.7	16

capacitance (C_{tun}) is adjusted to achieve the resonance frequency at 13.56 MHz. The coupling factor as a function of the distance must be taken into account in order to estimate the maximum read range. The coupling coefficient simulated for the antennas considered in the reader is modeled in the simulator using a linear fit in log scale. The tag inductance and quality factor reduction due to the proximity of the metal case of the smartphone is also taken into account, using a third order polynomial that fits the measured values. The AC voltage threshold is around 4.8 V, that corresponds to a received power of 13.7 dBm (for $R_{IC} = 450\ \Omega$). It is important to note the nonlinear behavior of the system. For received levels higher than this threshold, the received power increases and the resistance decreases due to the reduction of the on resistance of the transistors in the rectifier, and the effect of the RF limiter [33]. This low R_{IC} value has a secondary effect that is the reduction of the load modulation effect. The input impedance for small reader-tag distances changes due the coupling effect. At the resonance frequency, the input resistance at the reader is given by the reflected impedance $R_1 + k^2\omega_0 L_2 Q_{2L}$. Therefore, low values of R_{IC} or equivalently Q_{2L} result in a lower variation of the input impedance. The load modulation produces an input mismatch that reduces the transmitter power and therefore the received power and the efficiency.

Table 3 shows the simulated read range obtained for the three reader antenna cases. The importance of maximizing the coupling between the coils is fundamental to reach higher read ranges. The read range for Antenna 3 (Fig. 6c) is smaller due to its lower coupling coefficient. For transmission power of 20 dBm the effect of load modulation can be observed in the reader using this antenna, in which for very small distances the received power does not reach the threshold. However, this drawback is solved increasing the transmission power, integrating a transmitter in the smartphone.

The automatized setup to measure the magnetic field received at the antenna used in this work is shown in Fig. 10. It is composed by the reader (commercial smartphone, placed on a moving part controlled by a stepper motor, Nema 24), the antenna under test (50 × 50 mm, 6 loops), which is connected to the Vector Network Analyzer (VNA, Agilent E5062A) or to the Spectrum Analyzer (SA, Rhode & Schwarz FSP) by means of the switch MSP2T-18 from Mini-circuits, which is governed by a voltage supply (Agilent E3631A). The SA, the VNA and the power supply are connected to a

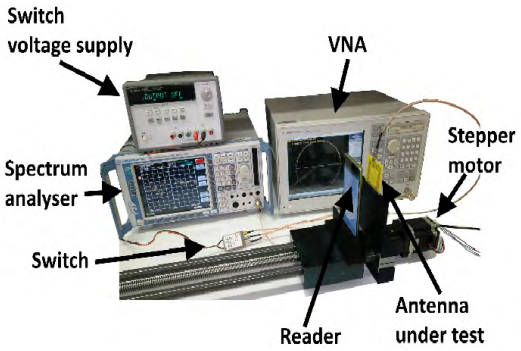

FIGURE 10. Setup to measure the magnetic field, composed by reader, antenna under test, spectrum analyzer, VNA, SPDT switch and voltage supply.

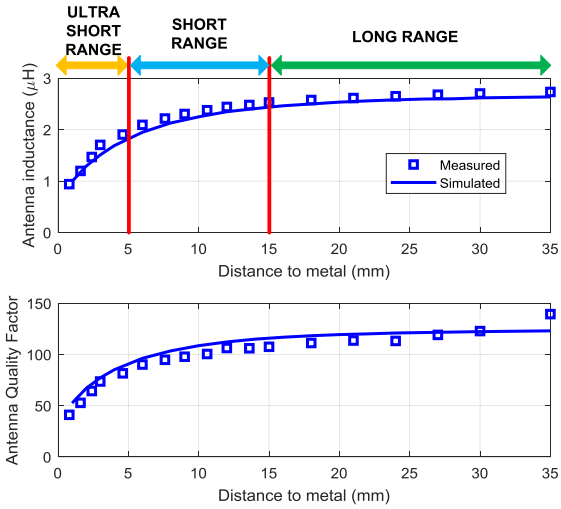

FIGURE 11. Measured (□) and simulated (solid line) inductance (a) and quality factor (b) of the loop antenna used in the prototype as a function of the distance to a metal plate.

computer through the General-Purpose Instrumentation Bus (GPIB), and the stepper motor through a Universal Serial Bus (USB). The procedure to control the instruments is programmed using a Matlab script, first selecting the appropriate voltage on the power supply to select the switch output, choosing the VNA to measure the S_{11} parameter, and then the SA to measure the power received at the operation frequency (13.56 MHz). Once the readings from the VNA and the SA are done, the stepper motor moves the reader 1 mm, and the process is repeated.

The reflection coefficient of the test antenna with a SMA connector is measured with a vector network analyzer (VNA). Fig. 11. compares the measured inductance and quality factor at 13.56 MHz as a function of the distance to a metal plane that simulates the effect of metallic parts of the mobile phone case. Good agreement is obtained between simulations and measurements taking into account the manufacturer tolerances. It is important to highlight that the inductance decreases when the loop antenna is close to metal, due to the induced image currents with opposite directions that reduce the magnetic flux. For distances greater than 15 mm

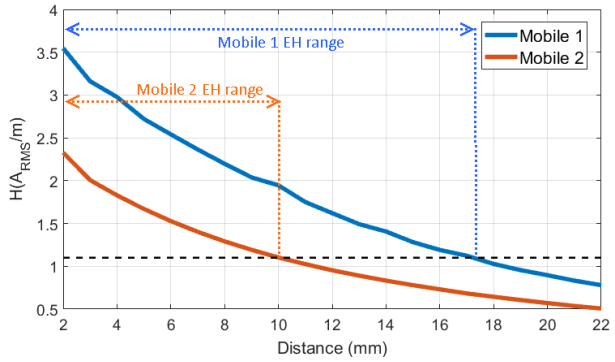

FIGURE 12. Measured average magnetic field as a function of the tag-to-reader distance for two mobile models. We can see that once the magnetic field goes below the threshold, voltage output falls to zero [36].

the inductance is nearly flat with an average value around 2.8 μH. Therefore, the resonance frequency of the tag can be tuned adding a tuning capacitor in parallel with the antenna. Depending of the value chosen, the tag can be designed to improve its operation for ultra-short, short or long ranges. In this work the selected distance is greater than 15 mm, because the coupling coefficient is lower than in the other cases and therefore the power received by the tag can be expected to be higher as it is close to the mobile. On the other hand the effect of detuning is compensated by this higher power value. In addition, when the tag is close to the mobile, the bandwidth of the system increases because the tag quality factor decreases. This is caused by the antenna quality factor reduction (as shown in Fig. 5) and by the decrease of the IC load resistance (due to higher power received by the tag).

Fig. 12 shows the H_{av} as a function of the distance for two mobiles. For the current consumption of the tag, a read range of between 1 cm and 2 cm is obtained, depending on which smartphone is used as a reader. This distance corresponds to a measured minimum magnetic field equal to 1.1 A_{RMS}/m [36, Fig. 6]. At the threshold distance, the measured power performed with the spectrum analyzer (that corresponds to the tag loaded with $R_L = 50\ \Omega$) is approximately 3 dBm. Similar read ranges are obtained in the simulations (Table 3), depending on the performance of the mobile used. The mobile 1 transmits higher power than the older model (mobile 2) and consequently the read range is noticeable higher.

C. TAG FIRMWARE

Fig. 13 shows a flow diagram of the system. The process is triggered by tapping the tag with the reader (i.e. the commercial smartphone), which supplies energy to the tag. If the energy received by the tag is higher than the threshold mentioned above, the rectified DC output of the NFC IC provides the energy supply to the tag chipset. Once the microcontroller is powered up, it sends the order to the sensor through the I^2C bus to sense the color. The sensor measures the RGB and sends it back to the microcontroller, which calculates the HSV color (see section III) and writes the result into the NFC IC EEPROM in NDEF (NFC Data Exchange Format)

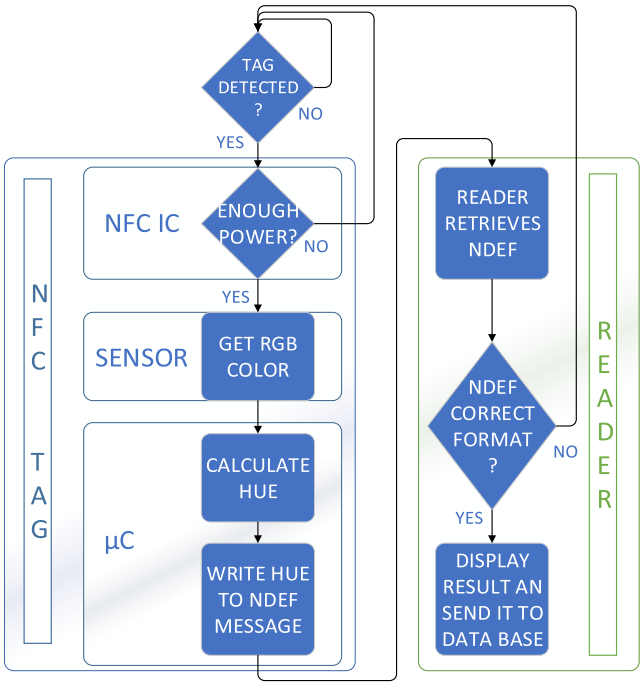

FIGURE 13. Flow diagram of the system, indicating the tag (left) and the reader (right).

format. Once the tag contains the NDEF message, this is used to modulate the signal that will be retrieved by the reader and an android app analyses the message to ensure that it is in the correct format and parses the information contained in the message. This obtains the measured HSV value and displays it on the screen together with the color representation. The android app calculates the pH based on a preconfigured calibration curve and sends the final result to an IoT database that records a history of the measurements.

The prototype presented has been designed including the pin accesses to program the microcontroller, (it can be seen at the top side of the tag on Fig. 3a). These pins can be connected to a programmer such an Arduino UNO with an ISP (In-System Programmer) code, allowing to upload the code from the Arduino IDE in an easy way, to adjust the calibration curve or the sampling timing if necessary. The developed firmware consists of an initialization code configuration which establishes the connection with the colorimeter sensor and with the NFC IC through I^2C bus. If the sensor is detected, the color measurement starts the loop mode while the chip is powered. The sampling loop process begins sending an I^2C sequence to interrogate the sensor, which answers sending the following parameters: the RGB value, the luminance and the color temperature reading. Then the RGB is transformed to HSV using the mathematical model exposed in [49]. The resulting value of Hue is then encapsulated in NDEF text format, and sent via I^2C to the NFC chip, which will keep the reading on its internal memory. This process is repeated every 500 ms up to the last reading. However, for convenience, the code could be modified to keep a sequence of readings. The extrapolation from Hue to pH is processed

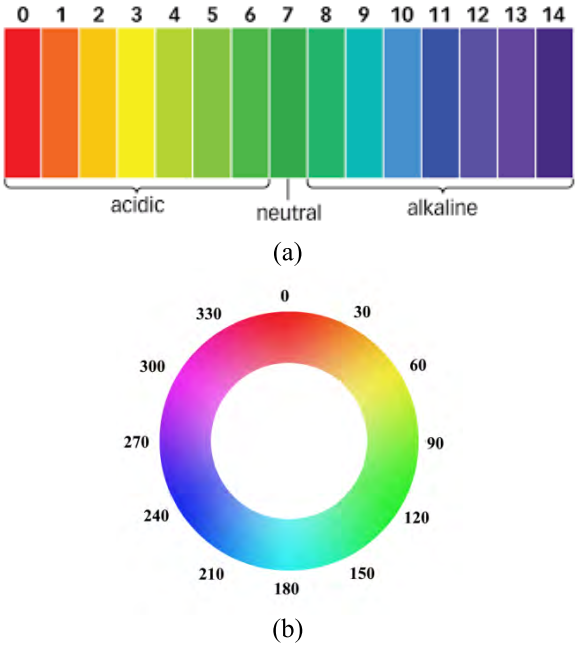

FIGURE 14. (a) pH as a function of the color of the paper strip. (b) Hue. Primary colors are at 0° (red), 120° (green), and 240° (blue).

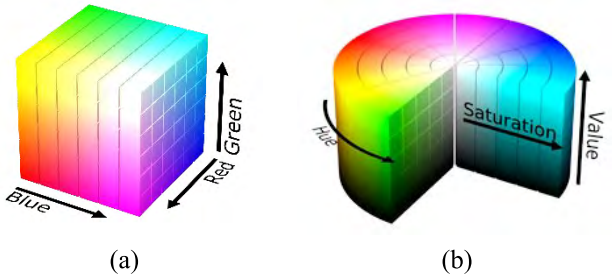

FIGURE 15. (a) RGB color space. (b) HSV color space.

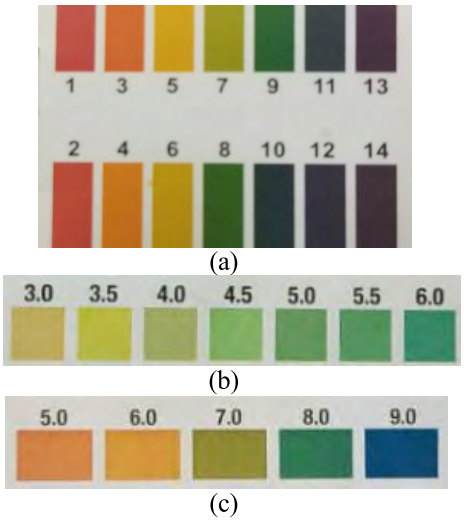

FIGURE 16. Color charts for the three paper strips tested: (a) chart for scale pH 1 to pH 14, (b) chart for scale pH 3 to pH 6, and (c) chart for scale pH 5 to pH 9.

on the reader (i.e. smartphone), since the calibration is configured from there. Although for this application only the RGB is used to calculate Hue, as mentioned above, the sensor provides luminance and color temperature, which could be easily added to the NDEF message and used for another type of color analysis.

III. SIGNAL PROCESSING

A mathematical model is needed to transform the raw color measurement in RGB provided by the color sensor into pH. However, a color model must be defined in order to digitalize a color for its representation or analysis. Several color models exist, the most common of which is the RGB. This additive color model is widely used for displays, while the CMYK is another additive color model that is widely used for color printing. Numerous other models also exist. Since color models are abstract mathematical models, it is possible to convert from one model to another.

Fig. 13a shows pH as a function of the color of the paper strip. We can see that the concentration of pH produces a change in color. One way to obtain the pH from the raw RGB measurement is to use a table-based method and an interpolation function. However, a simple model using HSV (Hue-Saturation-Value) color space is also available and found on the literature [50] [51]. This model is useful not only because it is more intuitive than raw RGB values but also because the conversions to and from RGB are extremely quick to compute and can be run in real time on the microcontroller. When shifts in colors have to be measured, the HSV (Hue Saturation Value) model should be considered. HSV is an alternative representation of RGB based on how the human eye works. Instead of measuring the portion of each primary color, the results are expressed in terms of Hue (representing pure color and expressed in degrees from 0° to 360°) (see Fig. 15), Saturation (percentage of white color), and Value (brightness, expressed in percentage).

From Fig. 14b, we expect there to be a simple relationship between Hue (angle) and pH. In this paper we have used the transformation given in [49] to transform RGB into hue using the following equations (8)-(9):

$$H = \begin{cases} \theta \rightarrow if B \leq G \\ 360 - \theta \rightarrow otherwise \end{cases} \tag{8}$$

where θ (in degrees) represents the Hue angle and R, G, and B are the values of red, green, and blue, respectively, in the 0 to 255 range.

$$\theta = arcos\left(\frac{\frac{1}{2}\left((R-G)+(R-B)\right)}{\sqrt{(R-G)^2+(R-B)\,(G-B)}}\right) \tag{9}$$

IV. EXPERIMENTAL RESULTS

To test the system, we compared the Hue obtained by measuring the color of the pH reactive strips with the NFC colorimeter and the pH obtained by a calibrated pH probe (Hanna Checker HI 98103). The pH probe was previously

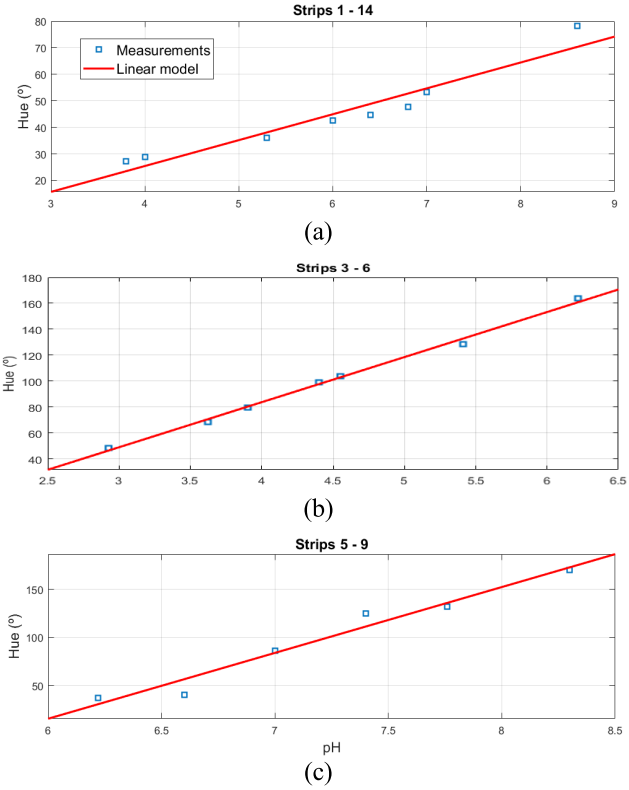

FIGURE 17. Hue measurements of several known pH values. (a) Strips 1 to 14, (b) strips 3 to 6:, and (c) strips 5 to 9.

calibrated using two reference solutions of pH 4 and 7. Three different paper strips with different pH ranges were tested. Fig. 16 shows the color charts of these pH paper strips. Fig. 16a shows the color palette of the full range strips from pH 1 to pH 14, while Fig. 16b and Fig. 16c correspond to the range's pH 3 to pH 6 and pH 5 to pH 9, respectively.

To verify the behavior of the strips, we measured several values of pH (see Fig. 17). This figure shows a linear behavior in the measured ranges.

Fig. 17 shows that the Hue of the strips behaves in a linear fashion, thus enabling the creation of a linear regression model (the red line in Fig. 17) to characterize each type of strip. Based on this linear model, the system can be calibrated by measuring two different pH values.

Since most current methods for determining the color of reactive strips are based on the image processing of a photograph of the strips [4]–[6], we compare the sensor color reading with the image processed by two different cameras. The main disadvantages of image processing systems are the variability in luminosity in the samples and the color correction applied to the pictures by each vendor. To compare the two methods, we took 30 measurements of four different strips. Fig. 18 shows the Hue calculated by placing and removing 30 times the strips from a 3D-printed enclosure specifically designed for the prototype presented in this paper (the black line with diamonds). The red and blue lines show the results of 30 pictures taken for each case at various distances (between 20 and 50 cm) and with smooth changes

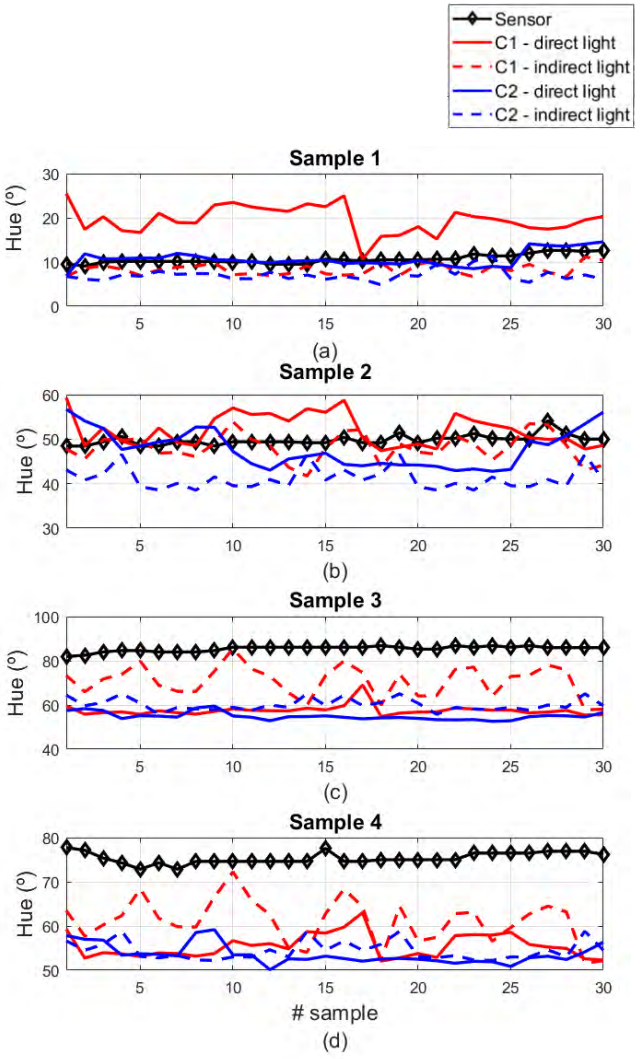

FIGURE 18. Comparison of Hue angle for 30 iterations of 4 different cases. (a) Strips from 1 to 14: pH 4, (b) strips from 1 to 14: pH 7, (c) strips from 3 to 6: pH 4 and (d) strips from 5 to 9: pH 7.

in angle. The images were taken by two different cameras in conditions of direct and indirect light for each (the continuous and dashed lines, respectively).

The pictures were taken at the maximum resolution for each camera (5488 × 4112 pixels for camera 1 and 5120 × 3840 pixels for camera 2). The images were analyzed using Matlab. The exact reactive part of the strips was selected manually. The average RGB was measured and converted to HSV using (8) and (9). This was therefore the same process as that used by image-processing systems.

We can see how the iterations measured with this system behaved linearly, since the lighting conditions and the distance between the sensor and the samples to be measured were always the same. For color analysis based on photography, on the other hand, these parameters were much more unstable.

Table 4 shows the standard deviation for each sample and each sensing method. The effects of different lighting

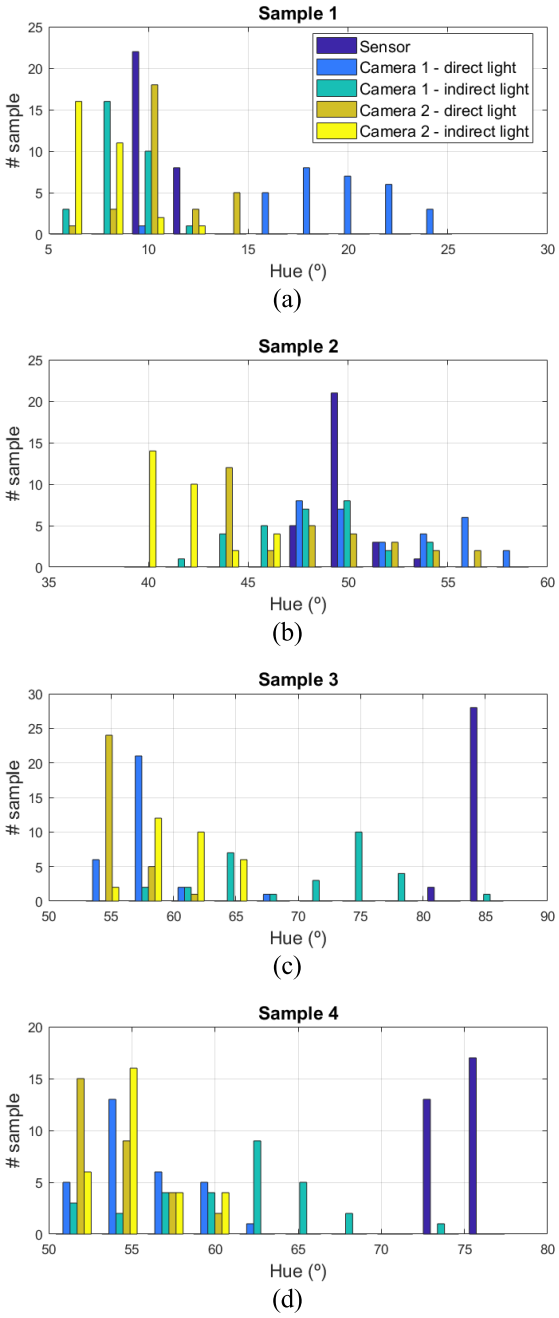

FIGURE 19. Histograms of measured values for 4 different cases. (a) Strips from 1 to 14: pH 4, (b) strips from 1 to 14: pH 7, (c) strips from 3 to 6: pH 4, and (d) strips from 5 to 9: pH 7.

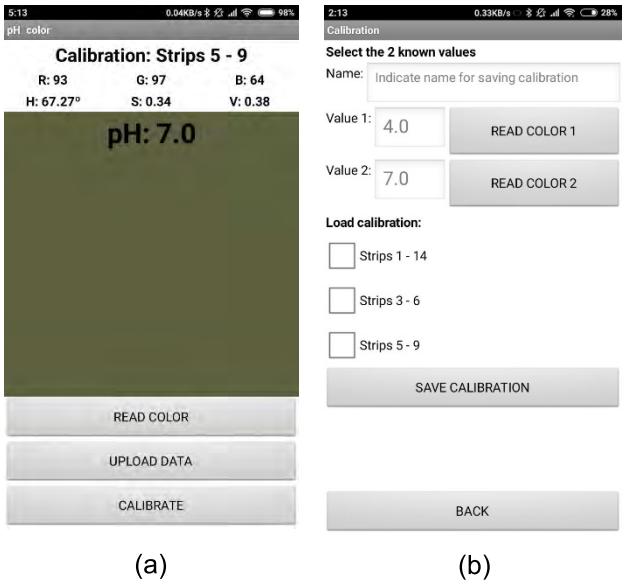

FIGURE 20. Designed Android APP: (a) main screen and (b) calibration screen.

FIGURE 21. Reading the color of a strip and calculating the pH with the Android application.

conditions and the deviation from accurate focus are quantified. As the mean values show, the results from camera 2 were better than those from camera 1. However, the best results were obtained with the proposed sensor.

To graphically represent the deviation observed when the same sample was measured several times, Fig. 19 shows the histograms for the values obtained. In all cases the sensor obtained the best results.

Although light plays an important role when measuring color, several other factors, including camera optics, image focusing, and processing software can also affect the reading. Moreover, systems based on image processing need complex software to detect which part of the image should be analyzed. For this reason, the proposed system can achieve better results: the conditions are always the same and the smartphone used to obtain the pH has no effect on the color reading. This system is therefore device-independent as well

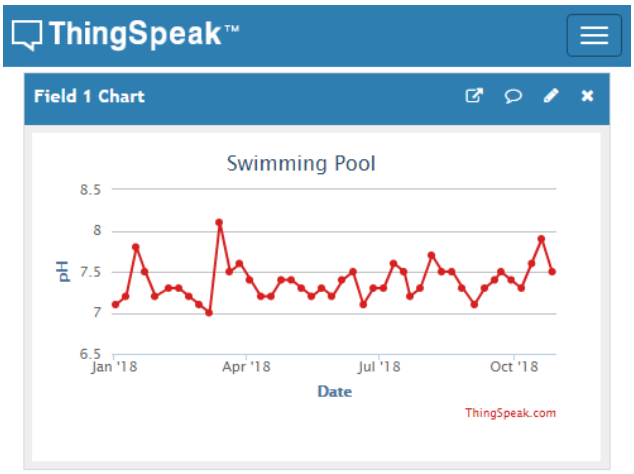

FIGURE 22. Cloud database showing the pH measurements of a swimming pool taken over several months.

TABLE 4. Hue Standard deviation (degrees).

	sample 1	sample 2	sample 3	sample 4	mean
Sensor	1.01	1.16	1.25	1.27	**1.17**
C1 direct light	3.19	3.62	2.47	2.74	**3.00**
C1 indirect light	1.27	3.16	7.03	5.08	**4.14**
C2 direct light	1.82	4.23	1.76	2.24	**2.51**
C2 indirect light	1.34	2.49	2.73	2.14	**2.18**

as simpler than other methods for determining the color of the reactive strips.

We have designed an Android application to display the results. This application reads the HSV values using the NFC protocol. Using the stored linear model, returns the pH. It also includes an option to calibrate strips from different manufacturers. For this purpose, two measurements for known pH values must be taken. The pH data are uploaded to a cloud database in order to store all historical measurements. Fig. 20a shows an image of the application's main screen, while Fig. 20b shows the calibration screen indicating the two known pH values used to calculate the linear function that will be used to estimate the pH of the measurements.

As well as showing the results, the app is programmed to upload the data to a database where the results are stored for further analysis and the historical measurements are kept. Fig. 21 shows the device with its 3D-printed enclosure and a strip. It also shows the smartphone used to power up the device and obtain the data and a display of the designed application.

As we mentioned earlier, as well as displaying the data, the application can upload the measurements to an IoT database. To show how this can be applied in a real scenario, Fig. 22 shows a graph on the ThingSpeak website that shows several measurements of the pH in a swimming pool. Historical measurements can thus be accessed from any device connected to the internet. This is an example of a weekly water analysis performed by the pool's maintenance staff. In this way the maintenance routine can be monitored to ensure that the pH is kept within an acceptable range for the swimming pool.

V. CONCLUSIONS

We have presented a batteryless, low-cost colorimeter integrated into an NFC tag. While this device has several applications, in this paper we apply it to the measurement of pH using pH-sensitive paper strips. Raw RGB measurements of the colorimeter IC are transformed into HSV color space. A simple linear relationship is found between pH and Hue for typical commercial strips. The pH is obtained from this line and can be easily calibrated using a known pH solution. We found that the repeatability of the measurement is higher than for methods based on smartphone cameras because the measurements are taken in controlled light conditions. We have designed a smartphone application to read the data from the NFC tag and send the pH to a cloud database. The theoretical and experimental read range obtained for the tag prototype is up to 18 mm depending on the smartphone used. This study shows that green sensors based on NFC IC with energy harvesting capabilities can help to design a new generation of low-cost smart devices and simplify the man-machine interface. Furthermore, new NFC chips are arriving to the market with better energy harvesting capabilities supplying more energy to the tag thus increasing NFC possibilities. This opens the door to cooperative IoT for smart cities and Industry 4.0 applications.

REFERENCES

[1] A. W. Martinez, S. T. Phillips, and G. M. Whitesides, "Diagnostics for the developing world: Microfluidic paper-based analytical devices," *Anal. Chem.*, vol. 82, no. 1, pp. 3–10, 2009.

[2] V. Oncescu, D. O. Dell, and D. Erickson, "Smartphone based health accessory for colorimetric detection of biomarkers in sweat and saliva," *Lab Chip*, vol. 13, no. 16, pp. 3232–3238, 2013.

[3] C. Sicard *et al.*, "Tools for water quality monitoring and mapping using paper-based sensors and cell phones," *Water Res.* vol. 70, pp. 360–369, Mar. 2015.

[4] N. K. Vuong, S. Chan, and C. T. Lau, "pH levels classification by colour quantization on a camera phone," in *Proc. IEEE Int. Conf. Commun. Mobile Comput.*, Shenzhen, China Apr. 2010, pp. 448–452.

[5] B. Y. Loh, N. K. Vuong, S. Chan, and C. T. , "Robust classification of pH levels on a camera phone," in *Proc. IMECS*, Hong Kong, Mar. 2011, pp. 600–604.

[6] S. D. Kim, Y. Koo, and Y. Yun, "A Smartphone-based automatic measurement method for colorimetric pH detection using a color adaptation algorithm," *Sensors*, vol. 17, no. 7, p. 1604, 2017.

[7] Y. Hashimoto, M. Hamaguchi, N. Nakanishi, A. Ohbora, T. Kojima, and M. Fukui, "Urinary pH is a predictor of diabetes in men; A population based large scale cohort study," *Diabetes Res. Clin. Pract.*, vol. 130, pp. 9–14, Aug. 2017.

[8] C. G. McCarty and E. Vitz, "pH Paradoxes: Demonstrating that it is not true that pH = -log[H+]," *J. Chem. Educ.*, vol. 83, no. 5, pp. 752–757, 2006.

[9] H. Wickström *et al.*, "Handheld colorimeter as quality control tool for inkjet printed flexible levothyroxine doses for pediatric use," *Int. J. Pharmaceutics*, vol. 536, no. 2, pp. 508–509, 2018.

[10] R. B. Dominguez, M. A. Orozco, G. Chávez, and A. Márquez-Lucero,, "The evaluation of a low-cost Colorimeter for glucose detection in salivary samples," *Sensors*, vol. 17, no. 11, p. 2495, 2017.

[11] P. Escobedo *et al.*, "Flexible passive near field communication tag for multigas sensing," *Anal. Chem.*, vol. 89, no. 3, pp. 1697–1703, 2017.

[12] *Near field communications forum. Available online*. Accessed: Jan. 17, 2019. [Online]. Available: http://nfc-forum.org
[13] K. Finkenzeller and D. Müller. *RFID Handbook: Fundamentals and Applications in Contactless Smart Cards, Radio Frequency Identification and Near-Field Communication*. Hoboken, NJ, USA: Wiley, 2010.
[14] D.Paret, *Design Constraints for NFC Devices*. Hoboken, NJ, USA: Wiley, 2016.
[15] E. Strommer, J. Kaartinen, J. Parkka, A. Ylisaukko-oja, and I. Korhonen, "Application of near field communication for health monitoring in daily life," in *Proc. Int. Conf. IEEE Eng. Med. Biol. Soc.*, New York, NY, USA, Sep. 2006, pp. 3246–3249.
[16] A. J. Jara, P. Lopez, D. Fernandez, M. A. Zamora, B. Ubeda, and A. F. Skarmeta, "Communication protocol for enabling continuous monitoring of elderly people through near field communications," *Interacting Comput.*, vol. 26, no. 2, pp. 145–168, 2013.
[17] M. Boada, A. Lázaro, R. Villarino, and D. Girbau, "Battery-less soil moisture measurement system based on a NFC device with energy harvesting capability," *IEEE Sensors J.*, vol. 18, no. 13, pp. 5541–5549, Jul. 2018.
[18] M. D. Steinberg, P. Kassal, I. Kerekovic, and I. M. Steinberg, "A wireless potentiostat for mobile chemical sensing and biosensing," *Talanta*, vol. 143, pp. 178–183, Oct. 2015.
[19] F. Carré, J. Caudeville, R. Bonnard, V. Bert, P. Boucard, and M. Ramel, "Soil contamination and human health: A major challenge for global soil security," in *Global Soil Security. Progress in Soil Science*. Edinburgh, U.K.: Springer, 2017, pp. 275–295.
[20] Y. Faruk "Potential ambient energy-harvesting sources and techniques," *J. Technol. Stud.*, vol. 35, no. 1, pp. 40–48, 2009.
[21] S. Kim *et al.*, "Ambient RF energy-harvesting technologies for self-sustainable standalone wireless sensor platforms," *Proc. IEEE*, vol. 102, no. 11, pp. 1649–1666, Nov. 2014.
[22] A. Lazaro, R. Villarino, and D. Girbau, "A survey of NFC sensors based on energy harvesting for IoT applications," *Sensors*, vol. 18, no. 11, p. 3746, Nov. 2018.
[23] J. M. Vicente, E. Avila-Navarro, C. G. Juan, N. García, and J. M. Sabater-Navarro, "Design of a wearable bio-patch for monitoring patient's temperature," in *Proc. 38th Annu. Int. Conf. IEEE Eng. Med. Biol. Soc. (EMBC)*, Orlando, FL, USA, Aug. 2016, pp. 4792–4795.
[24] H. Jeong *et al.*, "NFC-enabled, tattoo-like stretchable biosensor manufactured by âĂIJcut-and-pasteâĂİ method," in *Proc. 39th Annu. Int. Conf. IEEE Eng. Med. Biol. Soc. (EMBC)*, Seogwipo, South Korea, Jul. 2017, pp. 4094–4097.
[25] D. P. Rose *et al.*, "System-level design of an RFID sweat electrolyte sensor patch," in *Proc. 36th Annu. Int. Conf. IEEE Eng. Med. Biol. Soc.*, Chicago, IL, USA, Aug. 2014, pp. 4038–4041.
[26] R. Rahimi, U. Brener, M. Ochoa, and B. Ziaie, "Flexible and transparent pH monitoring system with NFC communication for wound monitoring applications," in *Proc. 30th Int. Conf. Micro Electro Mech. Syst. (MEMS)*, Las Vegas, NV, USA, Jan. 2017, pp. 125–128.
[27] P. Kassal, M. Zubak, G. Scheipl, G. J. Mohr, M. D. Steinberg, and I. M. Steinberg, "Smart bandage with wireless connectivity for optical monitoring of pH," *Sens. Actuators B, Chem.*, vol. 246, pp. 455–460, Jul. 2017.
[28] J. M. Azzarelli, K. A. Mirica, J. B. RavnsbÃęk, and T. M. Swager, "Wireless gas detection with a smartphone via rf communication," *Proc. Nat. Acad. Sci. USA*, vol. 111, no. 51, pp. 18162–18166, Dec. 2014.
[29] C. Kollegger *et al.*, "A system-on-chip NFC bicycle tire pressure measurement system," in *Proc. IEEE 60th Int. Midwest Symp. Circuits Syst. (MWSCAS)*, Aug. 2017, pp. 60–63.
[30] P. Kassal, I. M. Steinberg, and M. D. Steinberg, "Wireless smart tag with potentiometric input for ultra low-power chemical sensing," *Sens. Actuators B, Chem.*, vol. 184, pp. 254–259, Jul. 2013.
[31] *TCS3472 Color Light-TO-Digital Converter with IR Filter, TAOS135 Aug. 2012*. Accessed: Jan. 17, 2019. [Online]. Available: https://cdn-shop.adafruit.com/datasheets/TCS34725.pdf
[32] J. I. Agbinya, *Wireless Power Transfer*. Delft, The Netherlands: River Publishers, 2016.
[33] A. Costanzo, M. Dionigi, F. Mastri, M. Mongiardo, J. A. Russer, and P. Russer, "Rigorous network modeling of magnetic-resonant wireless power transfer," *Wireless Power Transf.*, vol. 1, no. 1, pp. 27–34, 2014.
[34] M. Gebhart, "Analytical considerations for an ISO/IEC14443 compliant SmartCard transponder," in *Proc. 11th Int. Conf. Telecommun.*, Jun. 2011, pp. 9–16.
[35] M. Ishii and K. Komiyama, "A measurement method for the antenna factor of small loop antenna by measuring the input impedance," in *Proc. Conf. Precis. Electromagn. Meas.*, London, U.K., Jul. 2004, pp. 80–81.
[36] M. Boada, A. Lazaro, R. Villarino, E. Gil, and D. Girbau, "Near-field soil moisture sensor with energy harvesting capability," in *Proc. 48th Eur. Microw. Conf.*, Madrid, Spain, 2018, pp. 235–238.
[37] X. Qing and Z. N. Chen, "Proximity effects of metallic environments on high frequency RFID reader antenna: study and applications," *IEEE Trans. Antennas Propag.*, vol. 55, no. 11, pp. 3105–3111, Nov. 2007.
[38] H. Zhu, S. Lai, and H. Dai, "Solutions of metal surface effect for HF RFID systems," in *Proc. Int. Conf. Wireless Commun., Netw. Mobile Comput.*, Shanghai, China, 2007, pp. 2089–2092.
[39] M. Gebhart, R. Neubauer, M. Stark, and D. Warnez, "Design of 13.56 MHz smartcard stickers with ferrite for payment and authentication," in *Proc. IEEE 3rd Int. Workshop Near Field Commun.*, Hagenberg, Austria, Feb. 2011, pp. 59–64.
[40] H. T. Jensen and H. Lee, "Chassis NFC antenna booster," U.S. Patent 9 729 210, Aug. 8, 2017.
[41] B. Lee, B. Kim, and S. Yang, "Enhanced loop structure of NFC antenna for mobile handset applications," *Int. J. Antennas Propag.*, vol. 2014, no. 6, Apr. 2014, Art. no. 187029.
[42] J.-Q. Zhu, Y.-L. Ban, C.-Y.-D. Sim, and G. Wu, "NFC antenna with nonuniform meandering line and partial coverage ferrite sheet for metal cover smartphone applications," *IEEE Trans. Antennas Propag.*, vol. 65, no. 6, pp. 2827–2835, Jun. 2017.
[43] Q. Liu, J. Zhou, and D. Chen, "NFC antenna assembly," U.S. Patent 9 941 572, Apr. 10, 2018.
[44] A. Zhao and H. Chen, "Small size NFC antenna with high performance," in *Proc. IEEE Int. Symp. Antennas Propag. (APSURSI)*, Fajardo, Puerto Rico, Jul. 2016, pp. 1469–1470.
[45] H. Chen and A. Zhao, "NFC antenna for portable device with metal back cover," in *Proc. IEEE Int. Symp. Antennas Propag. (APSURSI)*, Fajardo, Puerto Rico, Jul. 2016, pp. 1471–1472.
[46] J.-Q. Zhu, Y.-L. Ban, C.-Y.-D. Sim, and G. Wu, "NFC antenna with nonuniform meandering line and partial coverage ferrite sheet for metal cover smartphone applications," *IEEE Trans. Antennas Propag.*, vol. 65, no. 6, pp. 2827–2835, Jun. 2017.
[47] M.-A. Chung and C.-F. Yang, "Miniaturized NFC antenna design for a tablet PC with a narrow border and metal back-cover," *IEEE Antennas Wireless Propag. Lett.*, vol. 15, no. 31, pp. 1470–1474, Dec. 2016.
[48] B. Lee and F. J. Harackiewicz, "Design of a simple structured NFC loop antenna for mobile phones applications," *Prog. Electromagn. Res.*, vol. 76, pp. 149–157, 2017.
[49] F. Pierre, J.-F. Aujol, A. Bugeau, and V.-T. Ta, "Luminance-Hue specification in the RGB space," in *Proc. Int. Conf. Scale Space Variational Methods Comput. Vis.* Cham, Switzerland: Springer, May 2015, pp. 413–424.
[50] N. Lopez-Ruiz *et al.*, "Smartphone-based simultaneous pH and nitrite colorimetric determination for paper microfluidic devices," *Anal. Chem.*, vol. 86, no. 19, pp. 9554–9562, 2014.
[51] S. Capel-Cuevas *et al.*, "A compact optical instrument with artificial neural network for pH determination," *Sensors*, vol. 12, no. 5, pp. 6746–6763, May 2012.

MARTI BOADA received the B.Sc. degree in telecommunications engineering from the Universitat Rovira i Virgili (URV), Tarragona, Spain, in 2012, and the M.Sc. degree in telecommunications engineering and management from the Universitat Politècnica de Catalunya, Barcelona, Spain, in 2014. He is currently pursuing the Ph.D. degree with the Department of Electronic Engineering, URV. His research interests focus on microwave devices and systems, with an emphasis on RFID, NFC, and wireless sensors.

ANTONIO LAZARO (M'07–SM'16) was born in Lleida, Spain, in 1971. He received the master's and Ph.D. degrees in telecommunication engineering from the Universitat Politècnica de Catalunya (UPC), Barcelona, Spain, in 1994 and 1998, respectively. He became a Faculty Member of UPC, where he currently teaches a course on microwave circuits and antennas. Since 2004, he has been a full-time Professor with the Department of Electronic Engineering, Universitat Rovira i Virgili, Tarragona, Spain. His research interests focus on microwave device modeling, on-wafer noise measurements, monolithic microwave integrated circuits, low-phase noise oscillators, MEMS, RFID, UWB, and microwave systems.

RAMON VILLARINO received the degree in telecommunications technical engineering from Ramon Llull University, Barcelona, Spain, in 1994, the degree in senior telecommunications engineering from the Universitat Politècnica de Catalunya (UPC), Barcelona, in 2000, and the Ph.D. degree from UPC, in 2004. From 2005 to 2006, he was a Research Associate with the Technological Telecommunications Center of Catalonia, Barcelona. He was a Researcher and an Assistant Professor with the Universitat Autònoma de Barcelona, from 2006 to 2008. Since 2009, he has been a full-time Professor with the Universitat Rovira i Virgili, Tarragona, Spain. His research activities focus on radiometry, microwave devices, and systems based on UWB, RFIDs, and frequency selective structures using metamaterials.

DAVID GIRBAU (M'04–SM'13) received the B.Sc. degree in telecommunication engineering, the master's degree in electronics engineering, and the Ph.D. degree in telecommunication from the Universitat Politècnica de Catalunya (UPC), Barcelona, Spain, in 1998, 2002, and 2006, respectively. From 2001 to 2007, he was a Research Assistant with UPC. From 2005 to 2007, he was a part-time Assistant Professor with the Universitat Autònoma de Barcelona. Since 2007, he has been a full-time Professor with the Universitat Rovira i Virgili, Tarragona, Spain. His research interests include microwave devices and systems, with an emphasis on UWB, RFIDs, RF-MEMS, and wireless sensors.